shortest range will be the strongest arrival at long ranges.

We finally display in Fig. 8.17(c) the arrival structure over depth at a range of 80 km. Again the various ducted and leaky arrivals are identified; in addition, we see two low-amplitude diffracted arrivals. It is evident that only a wave-theory-based pulse solution allows an unambiguous and complete dissection of a propagation situation as complex as the surface-duct problem considered here.

8.5.6 Acoustic Emission From Ice Fractures

As an example of strong doppler effect in the ocean, we consider the problem of recording acoustic emission from propagating fractures in an Arctic ice cover. This problem is of significant importance in relation to the use of acoustic remote sensing of ice mechanical processes, but it is also a particularly interesting physical problem due to the interplay of high fracture speeds and low phase- and group velocities of some of the dominant propagation modes in the ice cover.

To illustrate the dynamic fracture effects we use a simple environmental model. Thus, the ice cover is assumed to be a homogeneous and isotropic, elastic plate of constant thickness 4 m. The compressional and shear speeds are 3500 m/s and 1800 m/s, respectively, and the density is 900 kg/m^3. The attenuations are assumed to be 0.5 and 1.0 dB/λ for compression and shear, respectively. Since we are here concerned about relatively short ranges and travel times, refraction in the water will be insignificant, and the water column is represented by an infinite halfspace with constant sound speed 1438 m/s.

It is well established that the ice will support two fundamental modes which are never cut off: the supersonic, and therefore leaky, *compressional mode*, and the subsonic *flexural mode* [24]. At high frequencies the ice plate may support a large number of modes, with the cutoff frequency for the first higher order mode being approximately equal to the *thickness-shear frequency* for the plate [24, 25],

$$f_0 = \frac{c_s}{2H}, \tag{8.72}$$

where c_s is the shear speed and H is the ice thickness. For the present case, this translates into a cutoff frequency of $f_0 = 225 Hz$, below which only the two fundamental modes exist.

We consider the scenario illustrated in Fig. 8.19. A tensile (e.g. thermal) crack is initiated at time t=0 s and propagates with a constant speed of 800 m/s for a total period of 20 ms, yielding a final crack length of 16 m. The acoustic emission is recorded by 3 vertical geophones, denoted G1, G2 and G3, placed at a range of 200 m from the crack initiation point, at bearings 120°, 90° and 60°, respectively, relative to the fracture propagation direction.
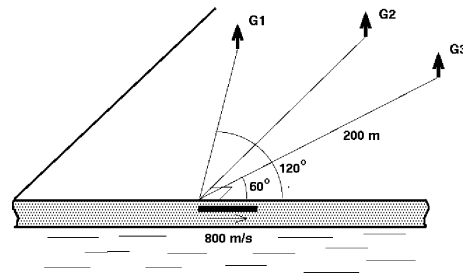
Fig. 8.19. Scenario for simulation of acoustic emission from propagating tensile crack in the Arctic ice cover. The crack tip is assumed to be at depth 1 m below the ice surface, and propagating with a horizontal speed of 800 m/s, over a total crack length of 16 m. The acoustic emission is recorded by three vertical geophones at a range of 200 m from the crack initiation point, at bearings $120°$, $90°$, and $60°$ relative to the crack propagation direction.
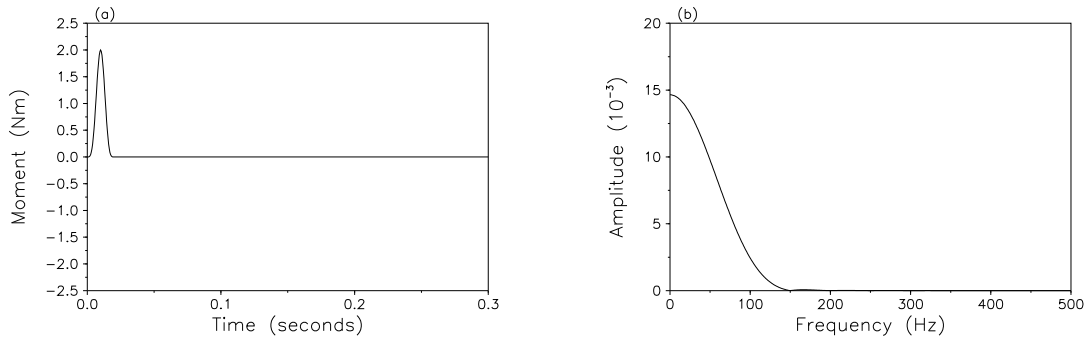

Fig. 8.20. Seismic moment representation of tensile crack. **(a)** Time series. **(b)** Frequency spectrum.
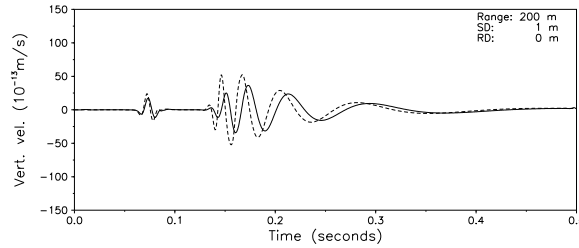
Fig. 8.21. Comparison of signals received on geophone G1 (solid curve) and geophone G2 (dashed curve). Relative to the receiver, the source is receding with radial velocity $v_s \cos \theta_s = -400$ m/s for G1, and 0 m/s for G2.
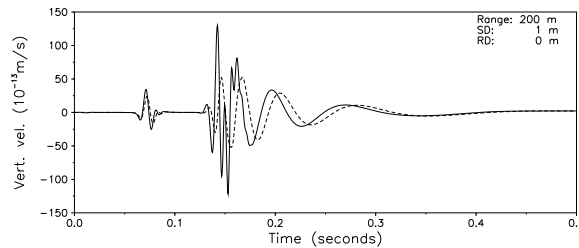

Fig. 8.22. Comparison of signals received on geophone G3 (solid curve) and geophone G2 (dashed curve). Relative to the receiver, the source is approaching with radial velocity $v_s \cos \theta_s = 400$ m/s for G3, and 0 m/s for G2.

The crack tip is represented by an omnidirectional seismic moment source, with a bell-shaped time dependence, as shown in Fig. 8.20(a). The associated frequency spectrum is shown in Fig. 8.20(b), indicating the dominant components to be at frequencies less than 150 Hz. This source representation is not necessarily realistic, but it contains all the fundamental physics necessary for illustrating the dynamic effects of the fracture propagation and the coupling to the ice modes.

Since the range to the receivers is large compared to the length of the crack, we will again use Eq. (8.58) to simulate the response. Figure 8.21 shows the resulting timeseries for geophones G1 (solid curve) and G2 (dashed curve). It is clear from the geometry in Fig. 8.20 that the crack tip is moving away from the receiver at a projected speed of 400 m/s, in our notation corresponding to $v_s \cos \theta_s = -400$ m/s, whereas within our approximations the source is at rest relative to geophone G2. A comparison of the two responses in Fig. 8.21 shows the expected frequency doppler shifts, both for the fundamental *compressional mode* arriving at $t = 0.06$ seconds, but much more clearly for the highly dispersive and slow fundamental *flexural mode* between $t = 0.12$

and $t = 0.5$ seconds. Another effect is a decrease in the observed amplitudes, primarily due to the longer mean range for geophone G1.

Similarly, Fig. 8.22 shows a comparison of the response of geophones G3 (solid curve) and G2 (dashed curve). For geophone G3 the crack tip is approaching with a projected speed of 400 m/s, i.e. $v_s \cos \theta_s = 400$ m/s, and here the differences is obviously much more dramatic than for G1. We clearly observe the expected effects of upward doppler shift and higher amplitudes for both fundamental modes. However, in addition we see a distinct high-frequency arrival interfering with the initial phase of the fundamental flexural wave. This is due to the excitation of a higher order mode in the ice. As described above, the cutoff frequency for the first higher order mode is 225 Hz. As a result, this mode was not observed on geophone G1 and G2 due to the fact that the source contains energy only up to 150 Hz, and the signal on G1 has a negative doppler shift. However, the relatively low phase velocity of the higher order mode, in combination with the high source speed, will produce a positive doppler shift in the forward direction, large enough to allow for its excitation, and therefore detection by geophone G3. This effect would clearly not be included in a modal expansion, ignoring cutoff effects and changes in mode shape.

Problems

8.1 Defining the *bandwidth* of a source wavelet as the total width of the main lobe of its frequency spectrum, show that the bandwidth of the wavelet

$$S(t) = \begin{cases} \frac{1}{2} \sin 2\pi f_c t \left(1 - \cos \frac{\pi}{2N} f_c t\right) & \text{for } 0 < t < 4N/f_c \\ 0 & \text{else} \end{cases},$$

is equal to f_c/N.

8.2 Using Fourier synthesis you have to compute a field produced by the source wavelet

$$S(t) = \begin{cases} \sin(2\pi f_c t) - \frac{1}{2} \sin(4\pi f_c t) & \text{for } 0 < t < 1/f_c \\ 0 & \text{else} \end{cases}.$$

a. Determine the frequency spectrum $S(f)$ of this wavelet.

b. At which frequency $f_{\max}$ would you truncate the computation of the Green's functions? Justify your answer.

c. The maximum time duration of the impulse response is $T_I = 15/f_c$. What is the frequency sampling required to avoid wrap-around in the computed response?

8.3 Assume you have a code for computing the transfer function $p(r, z, \omega)$ for the reflection problem in Fig. 8.2, which you want to use together with Fourier synthesis to model the transient response on a horizontal receiver array 100 m above the interface. The array has 11 elements at a spacing of 50 m, with the first element at $r = 0$.